


# Elastic Weyl Points and Surface Arc States in Three-Dimensional Structures

Xiaotian Shi,<sup>1</sup> Rajesh Chaunsali,<sup>1,2</sup> Feng Li,<sup>3</sup> and Jinkyu Yang<sup>1,\*</sup>

<sup>1</sup>*Aeronautics and Astronautics, University of Washington, Seattle, Washington 98195, USA*

<sup>2</sup>*LAUM, CNRS, Le Mans Université, Avenue Olivier Messiaen, 72085 Le Mans, France*

<sup>3</sup>*School of Physics and Optoelectronic Technology, South China University of Technology, Guangzhou, 510640 Guangdong, China*

 (Received 16 May 2019; revised manuscript received 5 August 2019; published 28 August 2019)

The study of Weyl points in electronic systems has inspired much recent research in classical systems such as photonic and acoustic lattices. Here we show how Weyl physics can also inspire the design of novel elastic structures. We construct a single-phase three-dimensional structure, an analog of the *AA*-stacked honeycomb lattice, and predict the existence of Weyl points with opposite topological charges ( $\pm 1$ ), elastic Fermi arcs, and the associated gapless topologically protected surface states. We apply full-scale numerical simulations on the elastic three-dimensional structure and present a clear visualization of topological surface states that are directional and robust. Such designed lattices can pave the way for novel vibration control and energy harvesting on structures that are ubiquitous in many engineering applications.

DOI: [10.1103/PhysRevApplied.12.024058](https://doi.org/10.1103/PhysRevApplied.12.024058)

## I. INTRODUCTION

Phononic crystals and metamaterials have shown new and exciting ways to control the flow of wave propagation in the medium [1–4]. Recently, the topology of band structures has emerged as a new design tool in this context. The essential idea is to characterize the bulk dispersion topologically and predict its effects on the edges or surfaces of the system. A nonzero topological invariant of the bulk usually implies the existence of edge or surface waves with nontrivial properties, such as directionality and robustness [5–7]. Several interesting strategies to manipulate elastic waves have been shown [8,9]. However, the studies so far focused mainly on one-dimensional and two-dimensional (2D) systems. It is not clear how a three-dimensional (3D) elastic structure could be designed to support topological surface states. What special characteristics those surface state would have and how they could be harnessed in engineering settings are some key questions. In this study, we attempt to address these questions by taking inspiration from Weyl physics.

Weyl semimetals [10–14] have recently attracted much attention for their exotic features. In Weyl semimetals, the Weyl point refers to the degeneracy point of two bands having linear dispersion in all directions in the 3D reciprocal space. The effective Weyl Hamiltonian is, in general, given by  $H(\mathbf{k}) = f(\mathbf{k})\sigma_0 + v_x k_x \sigma_x + v_y k_y \sigma_y + v_z k_z \sigma_z$ , where  $f(\mathbf{k})$  is an arbitrary real function and  $v_i$ ,  $k_i$ , and  $\sigma_i$  represent group velocity, momentum, and the Pauli

matrix, respectively. Weyl points behave as the sources or the sinks of the Berry curvature in the reciprocal space. By integrating the Berry flux on a sphere surrounding a Weyl point, we can get the nonvanishing topological charge (or Chern number) associated with it [15]. The Weyl point is robust against small perturbations and cannot be easily gapped unless it is annihilated with another Weyl point with the opposite topological charge [16]. For electronic systems, previous research has shown many unusual phenomena associated with Weyl points, such as robust surface states [10] and a chiral anomaly [17]. Later, Weyl physics was shown to be useful in the classical systems of photonic lattices [16,18–20] and acoustic lattices [21–27].

The implementation of Weyl physics in elastic structures, however, has been challenging so far. Recently, a self-assembled double gyroid structure that contains Weyl points for both electromagnetic and elastic waves was proposed [28]. Later, a design consisting of a thin plate and beams, which carries both Weyl and double-Weyl points, was also proposed [29]. In spite of these proposals, the experimental demonstration of elastic Weyl points remains elusive. Furthermore, there has not been a single study reporting full-scale numerical simulations in the elastic setting, by which Weyl physics can be directly visualized and appreciated. This is because such structures are extremely intricate to fabricate. At the same time, it is very demanding to computationally simulate their full-scale wave dynamics, because it involves several types of elastic modes.

In this research, we design a 3D elastic lattice made entirely of beams, which allow both translational and

\*jkyang@aa.washington.edu

rotational degrees of freedom along their length directions. We use finite-element analysis (FEA) to obtain a dispersion diagram for the unit cell and discuss its topological features in relation to Weyl physics. Inspired by widely used 3D hollow structures in engineering (e.g., a fuselage), we construct a full-scale hollow structure and show the existence of topological surface states in it. We also elucidate the relation of their directionality with the elastic Fermi arcs in the reciprocal space. We perform a transient simulation of the structure with a surface defect to numerically demonstrate the robust propagation of non-trivial surface waves. This study therefore paves the way for future research on the design and fabrication of Weyl-physics-based structures for engineering applications, such as vibration control and energy harvesting.

## II. DESIGN OF THE WEYL STRUCTURE

Previous studies in acoustics demonstrated the existence of Weyl points in a  $AA$ -stacked honeycomb lattice with chiral interlayer hopping [21]. A schematic of its nearest-neighbor tight-binding model is illustrated in Fig. 1(a). To make an equivalent mechanical system, we would need to use masses and springs that are connected by hinge joints. However, for a more-realistic design, we deviate from the spring-mass description and propose a unit cell made of beams as shown in Fig. 1(b). We take beam length  $L = 20$  mm and height  $P = 10$  mm. All in-plane beams (parallel to the  $x$ - $y$  plane) have square cross section of

width 3.0 mm, while out-of-plane beams have square cross section of width 0.7 mm to reduce the interlayer stiffness. We can still calculate the effective tight-binding Hamiltonian to analyze topological properties of our elastic structure (Appendix A). In Fig. 1(c), we show the first Brillouin zone with marked Weyl points at the high-symmetry points. These are of two opposite charges (Appendix A) and appear in the simulation results reported in the next section.

To conduct the numerical simulation, we use the commercial FEA software program ABAQUS. We model the beams using the Timoshenko beam elements. We follow the method used in Ref. [30] to apply periodic boundary conditions and construct frequency-band diagrams. We use stainless steel 316L as the structural material with elastic modulus  $E = 180$  GPa, density  $\rho = 7900$  kg/m<sup>3</sup>, and Poisson's ratio  $\nu = 0.3$ , which could be used for current 3D metal printing [31]. We ignore any material dissipation. The out-of-plane beams produce an effective synthetic gauge flux and break the effective time-reversal symmetry at a fixed  $k_z$ . Therefore, the system can be treated as an elastic realization of the topological Haldane model [32].

## III. RESULTS

### A. Weyl points in unit-cell dispersion

We show the band structure of the unit cell along the irreducible Brillouin zone at  $k_z = 0$  in Fig. 2(a). We observe that the 13th and 14th bands, predominately with out-of-plane polarization (see Appendix B), are degenerate at the  $K$  point around 6.12 kHz [see the rectangular box and the enlargement in the inset in Fig. 2(a)]. This is a Weyl point in the system, and it is the same as the yellow spheres in Fig. 1(c). We calculate the Weyl charge by fitting the dispersion diagram of a two-band Hamiltonian around the Weyl point (see the red curves in the inset). As a result, we obtain a Weyl charge of  $-1$  from this Weyl point (see Appendix A).

When we plot the dispersion diagram for  $k_z = \pi/2P$ , the degeneracy of the bands is lifted, and there emerges a band gap between the 13th band and the 14th band, as shown by the gray region in Fig. 2(b). We increase  $k_z$  further to plot the dispersion curves at  $k_z = \pi/P$  [Fig. 2(c)]. We observe that the band gap closes again, and the two bands establish a degeneracy at 5.34 kHz, but at the  $H$  point of the Brillouin zone instead of the  $K$  point. This is the second Weyl point in the system, and it corresponds to the purple markers in Fig. 1(c). As shown in the inset, we again use the two-band Hamiltonian to represent the dispersion characteristics around this Weyl point and find that the Weyl point has  $+1$  topological charge.

In Fig. 2(d), we plot the dispersion diagram along the  $K$ - $H$  direction to clearly visualize the Weyl degeneracy at the  $K$  and  $H$  points and the existence of a band gap between the 13th band and the 14th band when the  $k_z$  value

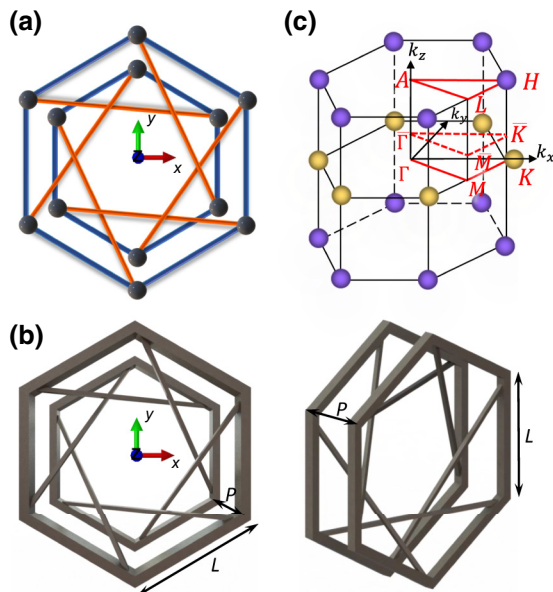


FIG. 1. (a)  $AA$ -stacked hexagonal lattice (blue) with chiral interlayer hopping (orange). (b) Top view (left) and slanted view (right) of the unit cell of the 3D elastic structure. (c) Illustration of the first Brillouin zone and Weyl points with opposite topological charges indicated by the yellow and purple spheres.

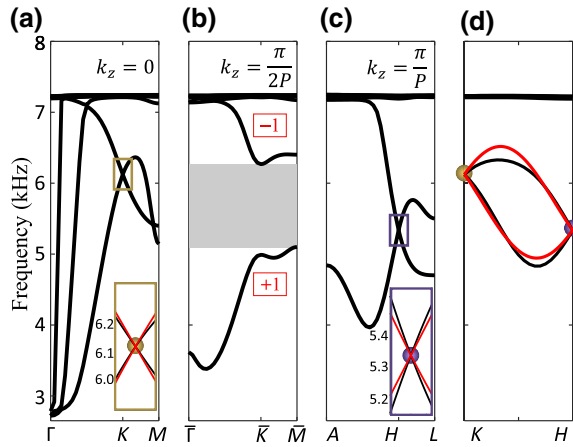


FIG. 2. Dispersion diagrams on the reduced reciprocal  $k_x$ - $k_y$  plane with fixed (a)  $k_z = 0$ , (b)  $k_z = \pi/2P$ , and (c)  $k_z = \pi/P$ . The yellow (purple) sphere refers to the Weyl point located at the  $K$  ( $H$ ) point with topological charge  $-1$  ( $+1$ ). The gray area in (b) represents a complete band gap. (d) Dispersion diagram along the  $K$ - $H$  line. The red and black curves are obtained from the two-band Hamiltonian and the FEA simulations, respectively.

lies somewhere in between. The two-band Hamiltonian (red curves) captures this evolution of the bands obtained through the FEA simulations (black curves) reasonably well. We use this effective Hamiltonian to numerically calculate the Chern numbers of the two bands above and below the band gap for a fixed  $k_z$ . For positive  $k_z$ , these are  $-1$  and  $+1$  for the upper and lower bands, respectively, as marked in Fig. 2(b). This indicates that the band gap is topologically nontrivial.

### B. Directional surface states in supercells

On the basis of the bulk-edge correspondence of topology, we expect topologically protected boundary modes arising at finite boundaries. To this end, we construct two

types of supercells, consisting of 15 unit cells each, having both armchair and zigzag types of finite boundaries. Figure 3(a) shows a schematic of how we choose the two types of supercells. For the zigzag supercell (see the slanted green box), we apply periodic boundary conditions in the  $x$  direction and the  $z$  direction. We use free boundary conditions at the top and bottom ends. We fix  $k_z = \pi/2P$  and plot the dispersion diagram in Fig. 3(b). We observe two modes inside the band gap, which are localized at the top (red) and the bottom (blue) ends of the supercell [see Fig. 3(d)]. From their slope we can conclude that the top-end (bottom-end) mode will have a negative (positive) group velocity in the  $x$  direction [see the green arrows in Fig. 3(a)].

Similarly, we study another supercell with the armchair type of boundaries [see the horizontal red box in Fig. 3(a)]. We show that it supports localized modes at the left and right ends [see Figs. 3(c) and 3(e)]. These left-end and right-end modes exhibit negative and positive group velocities, respectively [see the red arrows in Fig. 3(a)]. Therefore, it is straightforward to deduce that a wave packet injected at 5.4 kHz (shown as a star) on the surface of the full-scale lattice, having simultaneous zigzag and armchair boundaries, will travel counterclockwise for  $k_z = \pi/2P$ . In the same vein, we expect to obtain a traveling surface wave in the clockwise direction for  $k_z = -\pi/2P$ .

### C. Elastic Fermi arcs in the full-scale model

We now demonstrate the existence of surface states in a full-scale 3D structure. We choose a hollow structure for two reasons: (i) such structures are ubiquitous in applications and (ii) they require a reduced amount of computational time for numerical simulations compared with solid ones. Without fixing  $k_z$ , we first excite our system at 5.4 kHz in the  $z$  direction. In Figs. 4(a) and 4(b), we

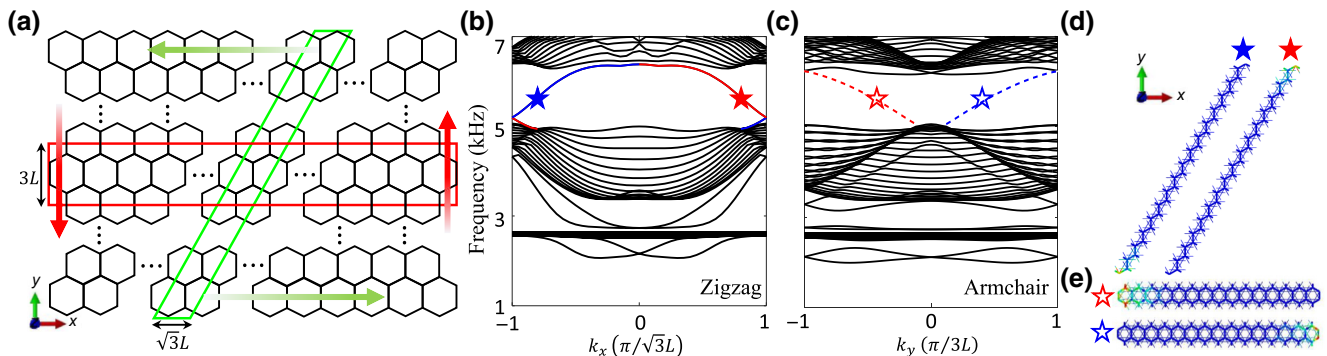


FIG. 3. (a) Supercells with zigzag-type (green box) and armchair-type (red box) boundaries. (b),(c) Band structure with fixed  $k_z = \pi/2P$  for the zigzag-type and armchair-type supercells, respectively. The red and blue curves represent the topological surface modes at the two opposite ends of the supercell. (d),(e) Mode shapes of the surface modes at 5.4 kHz corresponding to the solid and hollow stars in (b),(c). Color intensity represents the magnitude of total displacements.

show the  $z$  component of wave displacement when the force excitation is placed at the centers of the positive  $x$ - $z$  and negative  $y$ - $z$  planes, respectively (see the red stars in the insets). As we can see, the surface states propagate in particular directions and do not spread all across the whole plane. Especially in Fig. 4(b), the wave propagates in the  $y$  direction predominantly, reflecting the collimation effect [25].

For further investigation, we perform the fast Fourier transformation on the displacement field in the two spatial directions and plot the spectrum in Figs. 4(c) and 4(d). We observe arclike patterns of the peak spectral density (in yellow). These are called ‘‘Fermi arcs,’’ and also seen as the counterpart representation of the surface states in the reciprocal space. Since the normal vector to the Fermi arcs will determine the direction of the wave’s group velocity, we can deduce from Fig. 4(d) that the wave will propagate predominantly in the  $k_y$  direction given the straight

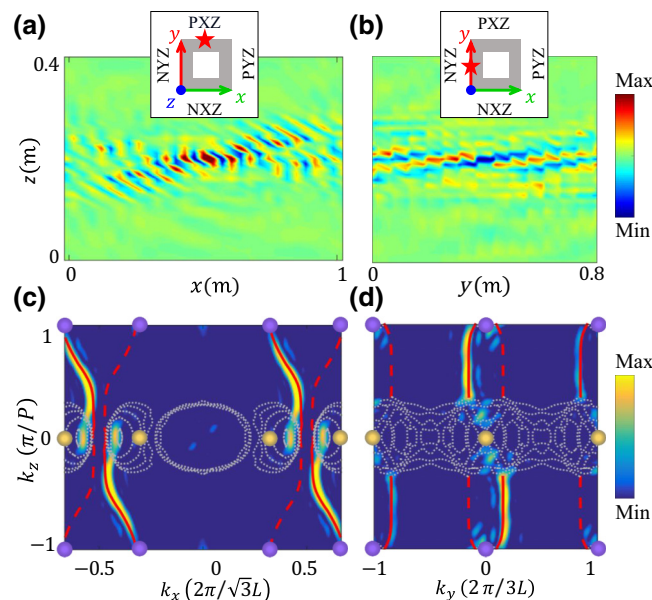


FIG. 4. Surface states and elastic Fermi arcs in a full-scale 3D hollow structure. (a),(b) Surface states under harmonic excitation at 5.4 kHz on the  $x$ - $z$  and  $y$ - $z$  planes, respectively. The point sources of excitation are placed in the center of each plane, as shown in the insets. The color intensity represents the nodal displacement in the  $z$  direction ( $u_z$ ). (c),(d) Spatial Fourier transforms of the field distributions of the surface states on the  $x$ - $z$  and  $y$ - $z$  planes, respectively. Spectral density shows the elastic Fermi arcs that connect the projections of the Weyl points with the opposite topological charges in the reduced 2D Brillouin zone. The solid red curves represent the simulated elastic Fermi arcs on the corresponding surfaces through supercell analysis, while the dashed curves indicate the Fermi arcs on the opposite surfaces. The projected bulk bands are shown as the dotted gray curves. NXZ, negative  $x$ - $z$  plane; NYZ, negative  $y$ - $z$  plane; PXZ, positive  $x$ - $z$  plane; PYZ, positive  $y$ - $z$  plane.

posture of the arc. This thus confirms the aforementioned collimation effect [Fig. 4(b)] in the wavevector space.

These Fermi arcs can also be obtained by equifrequency-contour analysis on the supercell (see details in Appendix C). To achieve this, we calculate the dispersion characteristics of the supercells, as shown in Figs. 3(b) and 3(c), for *all* values of  $k_z$  inside the first Brillouin zone. We then extract the wave numbers for 5.4 kHz to obtain the red curves in Figs. 4(c) and 4(d). Here the solid curves correspond to the solutions on the plane of excitation, while the dashed curves represent those on the opposite surface. Evidently, the solid red curves closely match the spectral density arcs obtained from the full-scale simulation. The Fermi arc generally connects the Weyl points of opposite charges [23], but here we see that they connect the two Weyl points (in purple and yellow) roughly but not exactly. This is because the system supports the two Weyl points at different frequencies [see the frequency offset of the yellow and purple points in Fig. 2(d)]. Since the Weyl points with opposite charges at the  $K$  and  $H$  points will be projected to the same points on the  $k_x$ - $k_y$  plane, thus canceling each other, there will be no topological surface states existing on the  $x$ - $y$  surface [14,23].

#### D. Robust one-way propagation

We now proceed to the full-scale, transient numerical study performed at 5.4 kHz, but for a fixed  $k_z$ . Figure 5(a) shows the entire hollow structure, along with a rectangular defect on the  $x$ - $z$  surface, to demonstrate the robustness of surface states. The top view of the structure is shown in Fig. 5(b). We fix all the degrees of freedom of the nodes on the top and bottom layers. To ensure excitation with the desired  $k_z$ , we apply four-point force excitation in the  $z$  direction on the tenth to 13th layers on the  $y$ - $z$  plane [marked with red arrows in the inset in Fig. 5(a)]. We use a Gaussian-modulated sinusoidal pulse with a center frequency of 5.4 kHz, and we fix  $k_z = -\pi/2P$  by increasing the phase of the input signal by  $\pi/2$  from the tenth to the 13th layer. From the discussions above, we expect that the wave packet will propagate *clockwise* when looking from the top ( $z$  axis). In Figs. 5(c)–5(f), we plot the total displacement of the system at time  $t = 3.5$  ms,  $t = 5.5$  ms,  $t = 8$  ms, and  $t = 10$  ms, respectively. We observe that the elastic wave remains on the surface of the structure and travels upward only in the clockwise direction (viewing from the top) without obvious scattering or reflection at the corners [see Fig. 5(d) and the inset] or near the defects [see Fig. 5(e) and the inset, and also Movie 1 in Supplemental Material [33]]. This, therefore, demonstrates a robust one-way propagation of surface elastic waves in our Weyl structure. Similarly, we confirm the robustness of propagating waves inside the proposed structure [see Movie 2 in Supplemental Material [33]].

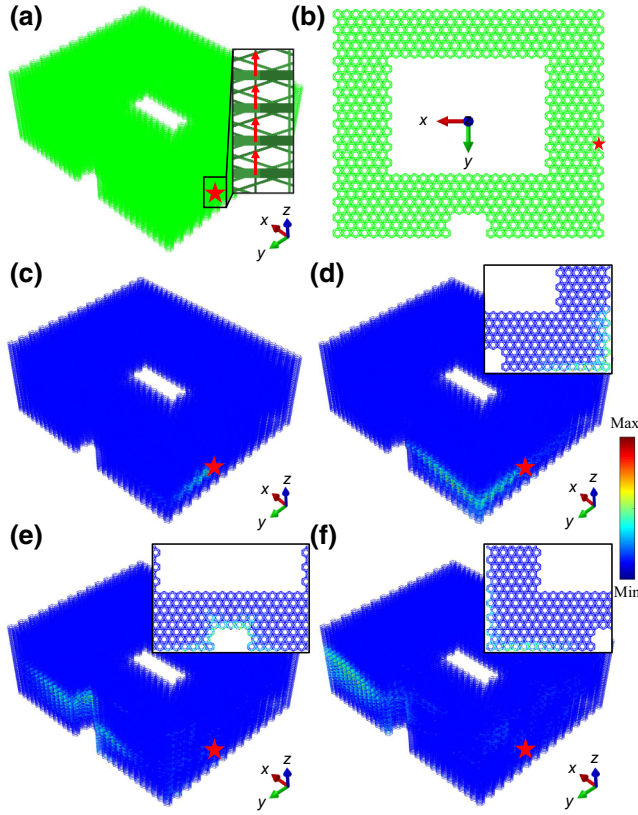


FIG. 5. Robust one-way surface state propagating in a 3D hollow structure. (a) Schematic and (b) top view of the 3D hollow sample with a surface defect on the  $x$ - $z$  surface. The red stars highlight the location of multipoint phased excitation. The exact locations of external loads are shown in the inset in (a). (c)–(f) The magnitude of total displacement of the surface elastic states at time  $t = 3.5$  ms,  $t = 5.5$  ms,  $t = 8$  ms, and  $t = 10$  ms, respectively. The insets in (d)–(f) show the cut views when the wave travels through the corner or defect at the 12th, 18th, and 25th layer, respectively.

#### IV. CONCLUSION

We design a 3D mechanical structure—analogue to the  $AA$ -stacked honeycomb lattice—by using slender beams. We show that this relatively simple design carries Weyl points at the vertices of the Brillouin zone. We use a two-band Hamiltonian model to describe the dynamics around the Weyl points and calculate their topological charges. We show the finite boundaries of this structure, both zigzag and armchair types, host localized states at fixed  $k_z$ . Using numerical simulations on a full-scale 3D structure, we show the existence of Fermi arcs and compare them with the results obtained from equifrequency-contour analysis. We highlight two unique wave phenomena in our structure: (i) collimation of the propagating elastic waves and (ii) robust one-way transport of elastic energy around the corners and defects. Our design could be easily scaled up or down, and can be relevant to applications such as

sensing, energy harvesting, and vibration control on 3D elastic structures.

#### ACKNOWLEDGMENTS

We thank Dr. Hyunryung Kim, Dr. Ying Wu, and Shuaifeng Li for fruitful discussions. X.S., R.C., and J.Y. are grateful for financial support from the U.S. National Science Foundation (Grants No. CAREER1553202 and No. EFRI-1741685).

#### APPENDIX A: TIGHT-BINDING MODEL OF $AA$ -STACKED GRAPHENE

We consider the tight-binding model of  $AA$ -stacked graphene with chiral interlayer coupling, as depicted in Fig. 1(a). The unit cell has an in-plane lattice constant  $L$  and out-of-plane lattice constant  $P$  in the  $z$  direction [see Fig. 1(b)]. Let the intralayer (interlayer) coupling be  $t_n$  ( $t_c$ ). Therefore, we write the Bloch Hamiltonian given by Refs. [16,21,27]

$$H(\mathbf{k}) = \begin{pmatrix} \varepsilon + t_c f(k_z P) & t_n \beta \\ (t_n \beta)^* & \varepsilon + t_c f(-k_z P) \end{pmatrix},$$

where  $\varepsilon$  denotes the on-site potential,  $\beta = e^{-ik_y L} + 2e^{ik_y L/2} \cos(\sqrt{3}k_x L/2)$ , and  $f(k_z P) = 2 \cos(\sqrt{3}k_x L - k_z P) + 4 \cos(3k_y L/2) \cos(\sqrt{3}k_x L/2 + k_z P)$ . By applying the  $k \times p$  method [16], we can expand the Hamiltonian near the  $K$  point [ $k_x = 4\sqrt{3}\pi/(9L)$ ,  $k_y = 0$ ,  $k_z = 0$ ] and obtain the effective Hamiltonian

$$H(\Delta\mathbf{k}) = (\varepsilon - 3t_c)\sigma_0 - \frac{3}{2}Lt_n(\Delta k_x \sigma_x - \Delta k_y \sigma_y) - 3\sqrt{3}Lt_c \Delta k_z \sigma_z,$$

where  $\Delta\mathbf{k} = (\Delta k_x, \Delta k_y, \Delta k_z)$  is a small  $\mathbf{k}$  vector deviating from the  $K$  point,  $\sigma_0$  is the  $2 \times 2$  unit matrix, and  $\sigma_x$ ,  $\sigma_y$ , and  $\sigma_z$  are the Pauli matrices.

We use  $\varepsilon = 5.73$  kHz,  $t_n = 0.875$  kHz, and  $t_c = -0.131$  kHz to fit the two-band dispersion with the curves obtained from the FEA results shown in Fig. 2. The effective Hamiltonian describes a Weyl point at the  $K$  point, whose topological charge is given by  $C = \text{sgn}(v_x v_y v_z)$ , where Dirac velocities  $v_x = -3Lt_n/2$ ,  $v_y = 3Lt_n/2$ , and  $v_z = -3\sqrt{3}Lt_c$ . Therefore,  $C = -1$  in this case. Similarly, by expanding the Hamiltonian at the  $H$  point [ $k_x = 4\sqrt{3}\pi/(9L)$ ,  $k_y = 0$ ,  $k_z = \pi/P$ ], we verify that there is another Weyl point with topological charge of  $+1$  located at the  $H$  point.

#### APPENDIX B: UNIT-CELL DISPERSION AND MODE POLARIZATION

Here we show the modes that are degenerate at the Weyl points are an *out-of-plane* type with a predominant

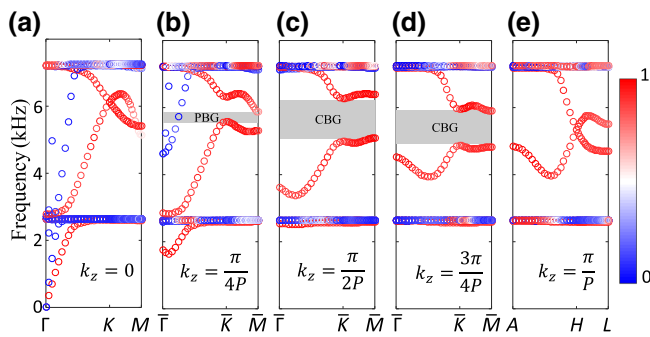


FIG. 6. Dispersion diagram of the unit cell in the  $k_x$ - $k_y$  plane at (a)  $k_z = 0$ , (b)  $k_z = \pi/4P$ , (c)  $k_z = \pi/2P$ , (d)  $k_z = 3\pi/4P$ , and (e)  $k_z = \pi/P$ . The color map represents the polarization factor  $P_z$ . The gray area in (b) represents a *partial* frequency band gap (PBG), while the gray zones in (c),(d) refer to *complete* band gaps (CBGs). The flat branches represent mainly the cases when the interlayer beams are locally resonant.

$z$  component. To this end, we define a polarization factor  $P_z = |U_z|^2 / (|U_x|^2 + |U_y|^2 + |U_z|^2)$  to distinguish bands with different polarization components, where  $U_x$ ,  $U_y$ , and  $U_z$  are the  $x$ ,  $y$ , and  $z$  components of the eigenvectors. Therefore, the out-of-plane modes, with predominately  $U_z$  component, will have a polarization factor close to unity, while the polarization factors of the in-plane modes will approach zero. We plot the bulk bands of the unit cell—colored with the information on the polarization factors—on the 2D reciprocal plane at various  $k_z$  values in Fig. 6. We can clearly see that the Weyl points are formed by the degeneracy of the two bands containing out-of-plane modes (in red).

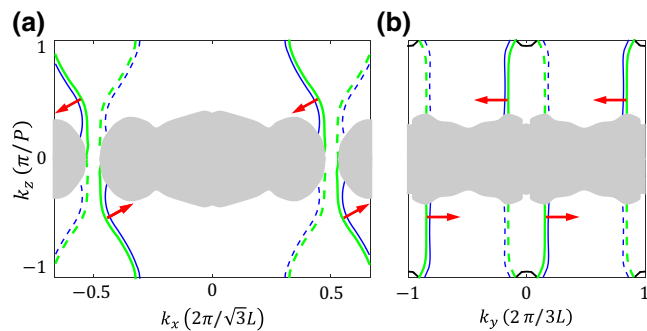


FIG. 7. (a) Equifrequency-contour plot of the supercell with zigzag-type boundaries at  $f = 5.4$  kHz (green) and  $f = 5.5$  kHz (blue). Red arrows show the normal vectors of the dispersion curves. Solid and dashed lines represents the mode in the forward and the opposite planes as indicated in Fig. 4. The gray regions refer to the projections of the bulk bands. (b) Similar results for the supercell with armchair-type boundaries.

## APPENDIX C: EQUIFREQUENCY-CONTOUR ANALYSIS

The equifrequency contours on the  $x$ - $z$  plane, as shown in Fig. 4(c), can be obtained by calculating the band structure of the supercell with the zigzag-type boundary. At  $f = 5.4$  kHz, we vary  $k_x$  from  $-4\pi/(3\sqrt{3}L)$  to  $4\pi/(3\sqrt{3}L)$  and  $k_z$  from  $-\pi/P$  to  $\pi/P$  to obtain wavevector plots as shown in green in Fig. 7(a). We show another equifrequency plot, obtained at slightly higher frequency ( $f = 5.5$  kHz), in blue to get a sense of the normal vector (i.e., the group velocity shown by red arrows at  $k_z = \pm\pi/2P$ ). Similarly, the result for the  $y$ - $z$  plane, from the supercell with the armchair-type boundary, is shown in Fig. 7(b). This equifrequency-contour plot confirms the collimation effect in the  $k_y$  direction.

- [1] Z. Liu, X. Zhang, Y. Mao, Y. Y. Zhu, Z. Yang, C. T. Chan, and P. Sheng, Locally resonant sonic materials, *Science* **289**, 1734 (2000).
- [2] M. I. Hussein, M. J. Leamy, and M. Ruzzene, Dynamics of phononic materials and structures: Historical origins, recent progress, and future outlook, *Appl. Mech. Rev.* **66**, 040802 (2014).
- [3] M. Kadic, T. Bückmann, R. Schittny, and M. Wegener, Metamaterials beyond electromagnetism, *Rep. Prog. Phys.* **76**, 126501 (2013).
- [4] K. Bertoldi, V. Vitelli, J. Christensen, and M. van Hecke, Flexible mechanical metamaterials, *Nat. Rev. Mater.* **2**, 17066 (2017).
- [5] M. Z. Hasan and C. L. Kane, Colloquium: Topological insulators, *Rev. Mod. Phys.* **82**, 3045 (2010).
- [6] X.-L. Qi and S.-C. Zhang, Topological insulators and superconductors, *Rev. Mod. Phys.* **83**, 1057 (2011).
- [7] E. Prodan and H. Schulz-Baldes, *Bulk and Boundary Invariants for Complex Topological Insulators* (Springer International Publishing, Cham, 2016). arXiv:1510.08744.
- [8] S. D. Huber, Topological mechanics, *Nat. Phys.* **12**, 621 (2016).
- [9] G. Ma, M. Xiao, and C. T. Chan, Topological phases in acoustic and mechanical systems, *Nat. Rev. Phys.* **1**, 281 (2019).
- [10] X. Wan, A. M. Turner, A. Vishwanath, and S. Y. Savrasov, Topological semimetal and Fermi-arc surface states in the electronic structure of pyrochlore iridates, *Phys. Rev. B* **83**, 205101 (2011).
- [11] C. Fang, M. J. Gilbert, X. Dai, and B. A. Bernevig, Multi-Weyl Topological Semimetals Stabilized by Point Group Symmetry, *Phys. Rev. Lett.* **108**, 266802 (2012).
- [12] S.-Y. Xu *et al.*, Discovery of a Weyl fermion semimetal and topological Fermi arcs, *Science* **349**, 613 (2015).
- [13] A. A. Soluyanov, D. Gresch, Z. Wang, Q. Wu, M. Troyer, X. Dai, and B. A. Bernevig, Type-II Weyl semimetals, *Nature* **527**, 495 (2015).

- [14] N. P. Armitage, E. J. Mele, and A. Vishwanath, Weyl and Dirac semimetals in three-dimensional solids, *Rev. Mod. Phys.* **90**, 015001 (2018).
- [15] Z. Fang, N. Nagaosa, K. S. Takahashi, A. Asamitsu, R. Mathieu, T. Ogasawara, H. Yamada, M. Kawasaki, Y. Tokura, and K. Terakura, The anomalous hall effect and magnetic monopoles in momentum space, *Science* **302**, 92 (2003).
- [16] W.-J. Chen, M. Xiao, and C. T. Chan, Photonic crystals possessing multiple Weyl points and the experimental observation of robust surface states, *Nat. Commun.* **7**, 13038 (2016).
- [17] H. B. Nielsen and M. Ninomiya, The Adler-Bell-Jackiw anomaly and Weyl fermions in a crystal, *Phys. Lett. B* **130**, 389 (1983).
- [18] L. Lu, L. Fu, J. D. Joannopoulos, and M. Soljačić, Weyl points and line nodes in gyroid photonic crystals, *Nat. Photonics* **7**, 294 (2013).
- [19] L. Lu, Z. Wang, D. Ye, L. Ran, L. Fu, J. D. Joannopoulos, and M. Soljačić, Experimental observation of Weyl points, *Science* **349**, 622 (2015).
- [20] M.-L. Chang, M. Xiao, W.-J. Chen, and C. T. Chan, Multiple Weyl points and the sign change of their topological charges in woodpile photonic crystals, *Phys. Rev. B* **95**, 125136 (2017).
- [21] M. Xiao, W.-J. Chen, W.-Y. He, and C. T. Chan, Synthetic gauge flux and Weyl points in acoustic systems, *Nat. Phys.* **11**, 920 (2015).
- [22] Z. Yang and B. Zhang, Acoustic Type-II Weyl Nodes from Stacking Dimerized Chains, *Phys. Rev. Lett.* **117**, 224301 (2016).
- [23] F. Li, X. Huang, J. Lu, J. Ma, and Z. Liu, Weyl points and Fermi arcs in a chiral phononic crystal, *Nat. Phys.* **14**, 30 (2018).
- [24] T. Liu, S. Zheng, H. Dai, D. Yu, and B. Xia, Acoustic semimetal with Weyl points and surface states, arXiv:1803.04284 [Cond-Mat] (2018).
- [25] H. Ge, X. Ni, Y. Tian, S. K. Gupta, M.-H. Lu, X. Lin, W.-D. Huang, C. T. Chan, and Y.-F. Chen, Experimental Observation of Acoustic Weyl Points and Topological Surface States, *Phys. Rev. Appl.* **10**, 014017 (2018).
- [26] H. He, C. Qiu, L. Ye, X. Cai, X. Fan, M. Ke, F. Zhang, and Z. Liu, Topological negative refraction of surface acoustic waves in a Weyl phononic crystal, *Nature* **560**, 61 (2018).
- [27] X. Zhang, M. Xiao, Y. Cheng, M.-H. Lu, and J. Christensen, Topological sound, *Commun. Phys.* **1**, 97 (2018).
- [28] M. Fruchart, S.-Y. Jeon, K. Hur, V. Cheianov, U. Wiesner, and V. Vitelli, Soft self-assembly of Weyl materials for light and sound, *PNAS* **115**, E3655 (2018).
- [29] Y.-T. Wang and Y.-W. Tsai, Multiple Weyl and double-Weyl points in an elastic chiral lattice, *New J. Phys.* **20**, 083031 (2018).
- [30] P. Wang, F. Casadei, S. H. Kang, and K. Bertoldi, Locally resonant band gaps in periodic beam lattices by tuning connectivity, *Phys. Rev. B* **91**, 020103 (2015).
- [31] C. S. Lefky, B. Zucker, D. Wright, A. R. Nassar, T. W. Simpson, and O. J. Hildreth, Dissolvable supports in powder bed fusion-printed stainless steel, *3D Print. Addit. Manuf.* **4**, 3 (2017).
- [32] F. D. M. Haldane, Model for a Quantum Hall Effect Without Landau Levels: Condensed-matter Realization of the “Parity Anomaly”, *Phys. Rev. Lett.* **61**, 2015 (1988).
- [33] See Supplemental Material at <http://link.aps.org/supplemental/10.1103/PhysRevApplied.12.024058> for surface-elastic-wave-propagation simulations on the outside (Movie 1) and inside (Movie 2) surfaces of the hollow 3D structure.